A&A 441, 289–302 (2005)
DOI: 10.1051/0004-6361:20047013

Astronomy & Astrophysics

The enigmatic B[e]-star Henize 2-90: the non-spherical mass loss history from an analysis of forbidden lines⋆,⋆⋆

M. Kraus[1], M. Borges Fernandes[1,2], F. X. de Araújo[2], and H. J. G. L. M. Lamers[1]

[1] Astronomical Institute, Utrecht University, Princetonplein 5, NL 3584 CC Utrecht, The Netherlands
e-mail: M.Kraus@phys.uu.nl; lamers@astro.uu.nl
[2] Observatório Nacional-MCT, Rua General José Cristino 77, 20921-400 São Cristovão, Rio de Janeiro, Brazil
e-mail: [borges; araujo]@on.br

Received 5 January 2004 / Accepted 29 April 2005

Abstract. We study the optical spectrum of the exciting B[e] star Hen 2-90 based on new high-resolution observations that cover the innermost 2″ of this object whose total extent is more than 3″. Our investigation is split in two parts, (i) a qualitative study of the presence of the numerous emission lines and classification of their line profiles, which indicate a circumstellar environment of high complexity, (ii) and a quantitative analysis of numerous forbidden lines, e.g. [OI], [OII], [OIII], [SII], [SIII], [ArIII], [ClII], [ClIII], and [NII]. We find correlation between the different ionization states of the elements and the velocities derived from the line profiles: the highly ionized atoms have the highest outflow velocity, while the neutral lines have the lowest. The recent HST image of Hen 2-90 (Sahai et al. 2002, ApJ, 573, L123) reveals a bipolar, highly ionized region, a neutral disk-like structure, and an intermediate region of moderate ionization. This HST image covers about the same innermost regions as our observations. When combining the velocity information with the HST image of Hen 2-90, it seems that a non-spherical stellar wind model is a good option to explain the ionization and spatial distribution of the circumstellar material. Such a wind might expand into the cavity formed during the AGB phase of the star, which is still visible as a large nebula, seen e.g. on Hα plates. We modelled the forbidden lines under the assumption of a non-spherically symmetric wind that can be split into a polar, a disk forming, and an intermediate wind, based on the HST image. We find that in order to fit the observed line luminosities, the mass flux, surface temperature, and terminal wind velocities need to be latitude dependent, which might be explained in terms of a rapidly rotating central star. A rotation speed of 75–80% of the critical velocity was derived from the terminal velocities extracted from the observed line wings considering the inclination of the system as suggested from the HST image. The total mass loss rate of the star was determined to be on the order of $3 \times 10^{-5}\ M_{\odot}\ \mathrm{yr}^{-1}$. The combination of this wind scenario and the underabundance of C, O, and N in comparison to the solar abundance of S, Ar, and Cl might be explained in terms of a rapidly rotating post-AGB star.

Key words. stars: mass-loss – ISM: planetary nebulae: individual: Hen 2-90 – line: identification – methods: data analysis

1. Introduction

Hen 2-90 (PN Sa 2-90, PN G305.1+01.4, IRAS 13064-6103) is a very interesting object whose evolutionary stage is unclear. Its distance was estimated to be about $d = 1.5$ kpc by Costa et al. (1993), while Sahai & Nyman (2000) adopted $d = 2.5$ kpc. Its effective temperature was estimated to be 51 000 K (Kaler & Jacoby 1991), and its luminosity was derived as $\log(L/L_{\odot}) \sim 3.0$ (Costa et al. 1993).

The star was first classified as a planetary nebula by Webster (1966) and Henize (1967). Later, Costa et al. (1993) and Maciel (1993) classified it as a planetary nebula with low metal abundance and with a central star of low mass and low luminosity. Lamers et al. (1998) included it in the list of objects presenting the B[e] phenomenon, as a compact planetary nebula B[e][1].

Sahai & Nyman (2000), based on HST images, and Guerrero et al. (2001), using ground-based images, have described the presence of a nebula bisected by a disk and with both a bipolar jet and knots, spaced uniformly. Guerrero et al. (2001) note that the dynamical stability of the jets and knots makes Hen 2-90 a unique object. These characteristics could point to a compact planetary nebula, since many planetary nebulae present a bipolar nebula. This fact implies that the asymmetries in the wind can already take place in the late stages of the AGB phase, where the jets can probably shape the

⋆ Based on observations done with the 1.52 m telescope at the European Southern Observatory (La Silla, Chile), under agreement with the Observatório Nacional-MCT (Brazil).

⋆⋆ Table 4 is only available in electronic form at http://www.edpsciences.org

[1] Note, that classification as a B star is based on the emission spectrum, but it does not reflect the effective temperature of the star.

spherical AGB wind in a bipolar scenario (Sahai & Trauger 1998; Imai et al. 2002; Vinković et al. 2004). However, the presence of a disk and jets could also be explained assuming that the system is a binary (Sahai & Nyman 2000). Guerrero et al. (2001) also noted based on near-IR colors, that Hen 2-90 might be a symbiotic system, i.e. a binary composed of a cool giant and a hot component with an accretion disk. Due to these two completely different interpretations (compact planetary nebula or symbiotic object) the real nature of Hen 2-90 remains unclear.

We study this object by means of high-resolution spectroscopy and low resolution spectrophotometry data obtained with the FEROS and B&C spectrographs, respectively, at the 1.52 m telescope in ESO (La Silla, Chile). The goals of this study are:

- to describe the spectral features in the optical spectrum obtained with a higher resolution than any other published observation to date, and
- to study the circumstellar material of this star (temperature and density distribution, velocities, ionization structure) using the spectrophotometrically calibrated line profiles.

For the first goal, we describe the various line profiles and associated Doppler velocities of the different types of lines. For the second, we make a complete analysis of all the forbidden emission lines (except for lines of FeII). In Sect. 2 we give information about our observations. In Sect. 3 we present a spectral atlas obtained from our optical data, showing the different line profiles identified in the spectra. In Sect. 4 we discuss whether the circumstellar material is located in a shell, nebula, or stellar wind. In Sect. 5 we derive the total mass loss rate of the star from modeling the forbidden emission lines in the scenario of a non-spherically symmetric wind. In Sect. 6 we discuss the validity of our assumptions and discuss the non-spherical wind scenario in terms of a rapidly rotating star. In addition, we discuss the nature of Hen 2-90, as being either a compact planetary nebula or a symbiotic object, based on abundance criteria found from the analysis and on spectral characteristics in our new high-resolution observations. In Sect. 7 we summarise our conclusions.

2. Observations and reductions

High and low resolution observations were obtained with the Fiber-fed Extended Range Optical Spectrograph (FEROS) and with the Boller & Chivens (B&C) spectrograph, respectively, at the ESO 1.52 m telescope in La Silla (Chile). FEROS is a bench-mounted Echelle spectrograph with the fibers located at the Cassegrain focus with a spectral resolution of $R = 48\,000$ corresponding to 2.2 pixels of 15 μm and with a wavelength coverage from 3600 Å to 9200 Å. The aperture of FEROS through which the fibers are illuminated is 2″.

High resolution observations of Hen 2-90 (higher than the spectra previously described in the literature) were taken on June 10, 2000, with an exposure time of 4800 s. These data were used to get a spectral atlas and a detailed description of the line profiles and also to deblend some features present in the low resolution spectra. The *S/N* ratio in the 5500 Å region is approximately 20. FEROS has a complete automatic on-line reduction, which we adopted. Equivalent widths were measured using an IRAF task that computes the line area above the adopted continuum.

Low resolution spectra of Hen 2-90 were taken on June 9, 2000, with an exposure time of 900 s. The slit width was 2″. The instrumental setup made use of grating #23 with 600 l mm^{-1}, providing a resolution of ∼4.6 Å in the range 3800−8700 Å. The efficiency of the CCD is a function of wavelength. It increases from about 70% at 3500 Å to its maximum value of 90% at about 7000 Å and then decreases again, reaching 75% at 8000 Å. This behaviour results in larger flux uncertainties of about 20% especially in the very low (<5000 Å) and very high (>7500 Å) wavelength regions of the spectrum, while in the range in between the flux uncertainties are more on the order of 10%. In the 5500 Å region, the *S/N* ratio in the continuum is approximately 40 for the B&C spectrum (hereafter Cassegrain spectrum). Since there is no completely line-free region in the spectrum, the *S/N* derived is an upper limit. The Cassegrain spectra were reduced using standard IRAF tasks, such as bias subtraction, flat-field normalization, and wavelength calibration. We did flux calibrations and extinction corrections with $E(B-V) = 1.3$ (Costa et al. 1993). Spectrophotometric standards from Hamuy et al. (1994) were used for absolute flux calibration. In the linearized spectra the line intensities were measured with the conventional method of adjusting a Gaussian function to the profile. Another source of uncertainty in the line intensities is the position of the underlying continuum and we estimated the errors to be about 20% for the weakest lines (line fluxes ≈10 on a scale with Hβ = 100) and about 10% for the strongest lines.

3. The spectral atlas

In order to identify the lines and make a spectral atlas of the optical region, we used the line lists provided by Moore (1945), Thackeray (1967), and Landaberry et al. (2001). We have also looked up two sites on the web: NIST Atomic Spectra Database Lines Form (URL `physics.nist.gov/cgi-bin/AtData/lines_form`) and The Atomic Line List v2.04 (URL `www.pa.uky.edu/peter/atomic/`).

Figure 1 shows the extinction corrected low resolution Cassegrain spectrum, which we can see is dominated by emission lines superimposed on a flat continuum. No absorption line is present. Table 4, which is only available in the online version of the journal, shows many emission lines that we have identified. There, the observed wavelength (Col. 1), the observed intensity ($I_{\rm obs}(\lambda)$, Col. 2), the extinction corrected intensity ($I_{\rm corr}(\lambda)$, Col. 3), and the proposed identification (Col. 4) for each line are given. The intensities are relative to Hβ = 100 with an observed Hβ flux of 2.18×10^{-12} ergs cm^{-2} s^{-1} and an extinction-corrected Hβ flux of 1.35×10^{-10} ergs cm^{-2} s^{-1}. The line identification given in Col. 4 of Table 4 encloses the ionization state of the element with the proposed transition and multiplet, as well as the rest wavelength of the transition. It is possible that more than one ion can be allocated to a

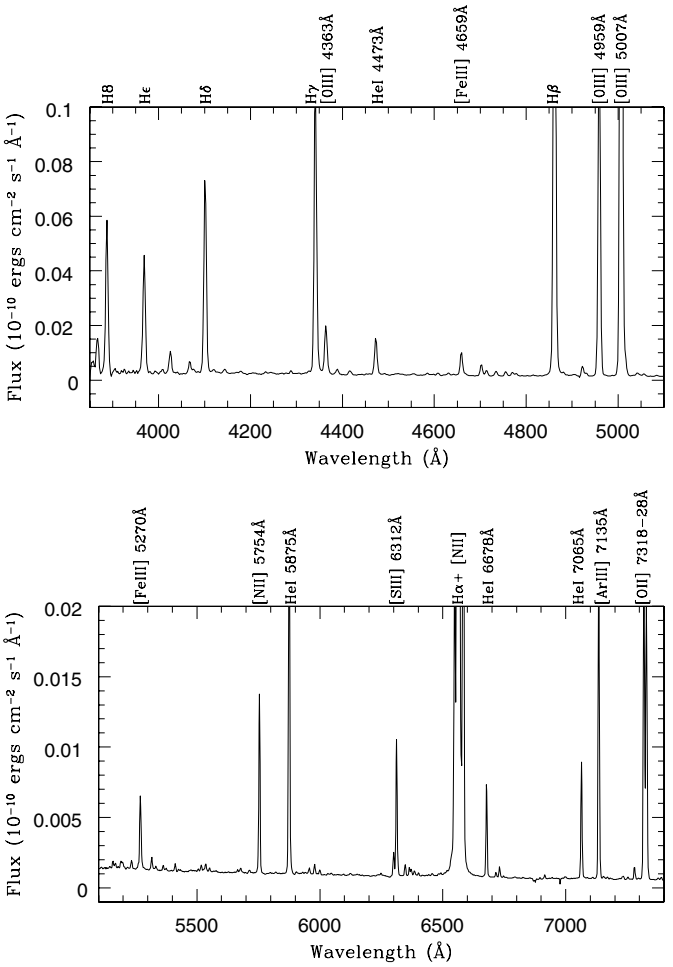

Fig. 1. Extinction corrected optical spectrum of Hen 2-90, observed with the B&C spectrograph.

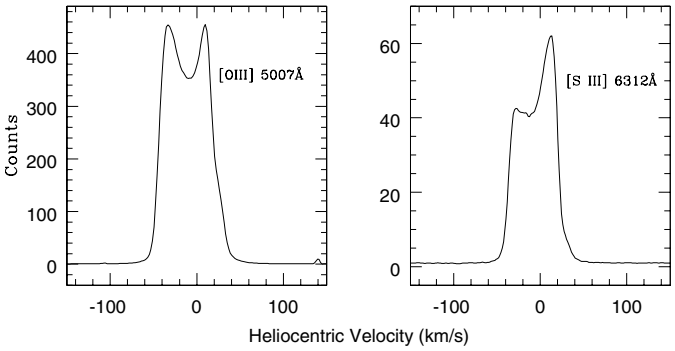

Fig. 2. The [O III] and [S III] lines taken from the Hen 2-90 high-resolution (FEROS) spectrum. They are only two examples of the presence of double-peaked emission line profiles. The velocities obtained from the wings of these lines are given in Table 1. Due to the strong lines, the high velocity wings are not resolved in this figure.

single feature. In these cases, we give some possible alternative identifications. For some lines no identification could be found, so they remain unidentified, labelled as "Uid" in the table.

Many permitted and forbidden lines were identified, most of them coming from singly or doubly ionized elements. Iron is by far the element with the richest spectrum, and [Fe III] lines are the strongest ones of this element, as cited by Guerrero et al. (2001). On the other hand, our data show an even larger number of permitted and forbidden lines of Fe II (although less intense than the [Fe III] lines), not reported by Guerrero et al. (2001).

The presence of very intense H I Balmer lines, He I, [O II], [O III], [N II], and [S III] lines is remarkable. Hα is the most intense line, followed by [O III] λ5007. This spectral characteristic is very curious, because it is different from that usually seen in a typical planetary nebula, where the [O III] λ 5007 is the most intense line. It also differs from the spectrum of a low-excitation planetary nebulae, where the Hα, Hβ, and [N II] $\lambda\lambda$6548,6583 are more intense than [O III] λ5007 (Kwok 2000). Guerrero et al. (2001) could neither confirm nor deny the presence of TiO absorption bands, the main signature of a symbiotic system, coming from the cool component. However, our spectrum clearly shows that the TiO bands are not present. In addition, we also could not identify the He II lines that would come from a hot component.

Identification of many Fe II permitted and forbidden lines, H I Balmer emission lines, and also [O I] lines confirms the presence of the B[e] phenomenon, described by Lamers et al. (1998). Concerning the line profiles, Guerrero et al. (2001) grouped the emission lines of Hen 2-90 into three groups: lines with (1) double peaks, (2) broad single peaks ($FWHM \geq 40$ km s^{-1}), and (3) narrow single peaks ($FWHM \leq 30$ km s^{-1}). Using our FEROS spectrum, we confirm the presence of those groups and define a new one, (4) the lines that clearly show a "shoulder", an intermediate case between the double peaks and the single peak. We list the lines falling into each profile group shortly and show an example:

(1) Double-peaked profiles are shown by the forbidden lines of O II, O III (left panel in Fig. 2), Ar III, Fe III, S III (right panel in Fig. 2), and Cl III with a peak separation of ~40 km s^{-1}. Also Hα shows a double-peak structure (Fig. 3). It is interesting to note that the asymmetric double-peaked lines have a more intense red peak than blue, indicating that the receding material is brighter than the approaching one. This finding agrees with Guerrero et al. (2001). However, contrary to these authors, our [O III] lines (except of the 4363 Å line) show double peaks with equal strength. The difference between the line profiles (and also the line intensities) is probably due to the different slit widths used for the observations.

The double-peaked forbidden lines show, in general, emission wings extending from 45 to around 100 km s^{-1} (except of Hα), indicating the presence of a low velocity wind. Hα, however, shows wings extending up to 1800 km s^{-1} (Fig. 4). Whether these wings indicate an outflow velocity or are produced due to electron scattering will be discussed in Sect. 5.4.

The velocity extent of the Hα wings, in our data, is higher than the 1050 km s^{-1} cited by Costa et al. (1993) and the 1500 km s^{-1} found by Guerrero et al. (2001). The differences in these measurements are due to different resolutions of the spectra and due to the different slit widths. However, only more observations with a similar instrumental setup can discard a spectral variation.

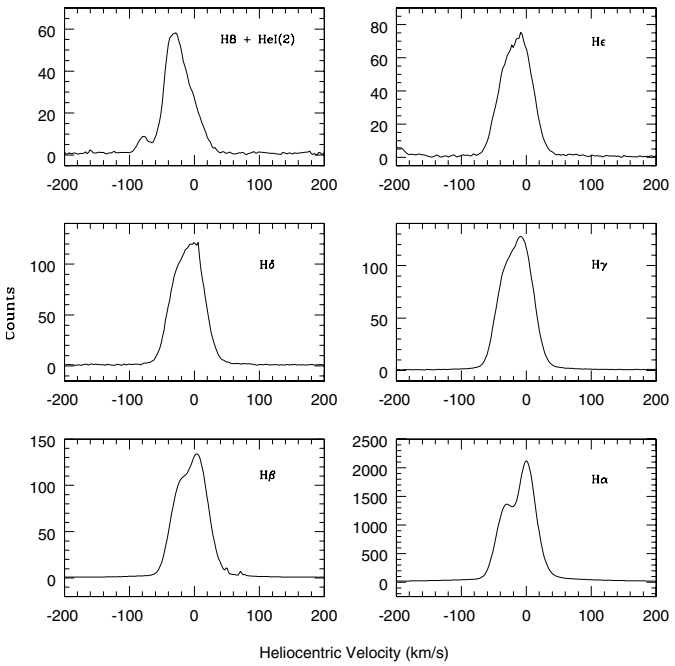

Fig. 3. The H I Balmer lines taken from the Hen 2-90 high-resolution (FEROS) spectrum. These lines show an evolution from single-peaked profiles over profiles with a shoulder to double-peaked profiles with decreasing quantum number.

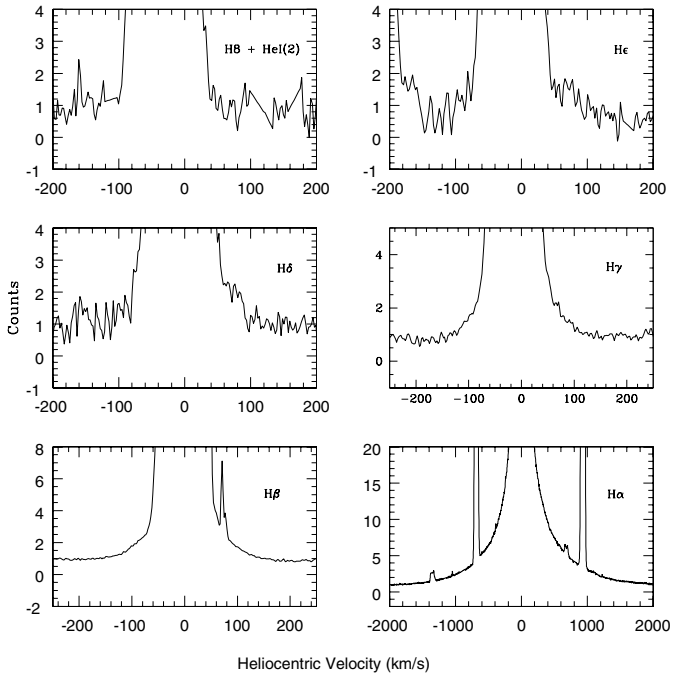

Fig. 4. Wings of the Balmer lines taken from the Hen 2-90 high-resolution (FEROS) spectrum. They show an increase in velocity from H8 to Hα (see Table 1). The wings of Hα extend to velocities around 1800 km s^{-1}; superimposed are the [N II] lines ($\lambda\lambda$6548,6583), as well as the only carbon line identified (C II, λ6578).

Another difference worth mentioning between our spectra and the data presented by Guerrero et al. (2001) is the absence of the [S III] λ6312 emission in their spectra. This line is very strong in our spectrum and shows double peaks (see Fig. 2). A possible explanation might be that, since this emission line arises in the outer parts of the intermediate wind (at least according to our non-spherical wind model, see Sect. 5.3 and Fig. 9), the slit width used by Guerrero et al. (2001) was too narrow to detect this line.

(2) Broad single-peaked profiles are found for Hδ, Hϵ, H8 (Fig. 3), Paschen lines, and some He I lines. The *FWHM* of these lines is typically $\geq$40 km s^{-1}.

(3) Narrow single-peaked profiles are shown, especially by the forbidden lines of Fe II and S II (Fig. 5). These lines typically have *FWHM* $\leq$ 30 km s^{-1}.

(4) Profiles with a "shoulder" or almost a second peak, which are in the new group identified by us. This group is represented by some He I, [N II], and [O I] lines (Fig. 6), as well as by Hβ and Hγ (Fig. 3). These lines are asymmetrical, and in some cases their blue and red wings show different velocities (see Table 1).

It is interesting to note that the H I Balmer lines show an evolution from a single peak in the high order lines to a double peak in Hα, having an intermediate case with shoulder in Hβ and Hγ (Fig. 3).

Table 1 shows the velocities derived from the maximum extend of the wings of several forbidden emission lines and some Balmer lines in our FEROS spectrum. There, the ion identification (Col. 1), laboratory wavelength (λ (Å), Col. 2), blue wing velocity ($v_{\rm blue}$ (km s^{-1}), Col. 3), and red wing velocity ($v_{\rm red}$ (km s^{-1}), Col. 4) for each line are given. Included are only lines whose velocities could be determined with high accuracy and which are not blended.

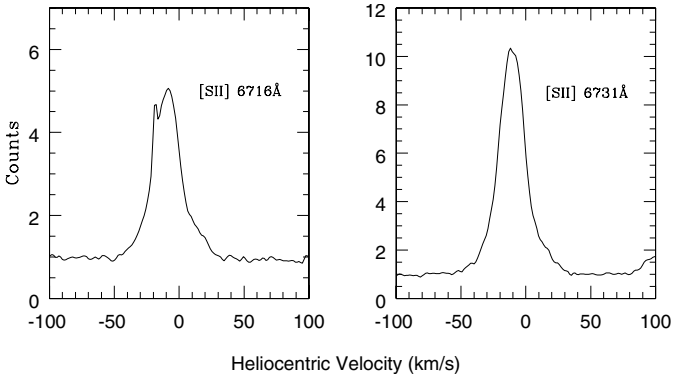

Fig. 5. [S II] line profiles present in the high-resolution spectrum (FEROS) of Hen 2-90. The derived wing velocities are given in Table 1.

In summary, we can say that compared with the Guerrero et al. (2001) data, our spectra revealed many more emission lines due to the higher signal-to-noise ratio (see Table 4). The fact that with the same applied reddening correction value some of the line profiles and intensities seem to have changed over a period of 6 months needs some further clarification. Our line profiles as shown were taken with FEROS using the fiber technique and with an aperture of 2″. A slit width of 2″ was also used for the Cassegrain spectrum from which we derived the line intensities. Guerrero et al. (2001) used a slit width of 1″, i.e. only half of our value. They therefore observed a region very close to the star, while our spectra cover a much larger

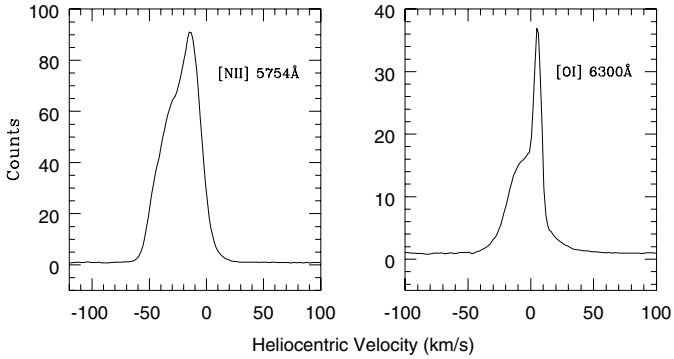

Fig. 6. The [N II] λ5754 and the [O I] λ6300 lines present in the Hen 2-90 high-resolution (FEROS) spectrum. Notice the presence of a "shoulder" or almost a second peak. The velocities obtained from the wings of these lines are given in Table 1.

Table 1. Derived maximum velocities where the blue and red wings reach the continuum. Listed are some forbidden emission lines and some Balmer lines in the FEROS spectrum whose maximum wing velocities could be determined well and which are not blended.

Ion	λ [Å]	$v_{\rm blue}$ [km s^{-1}]	$v_{\rm red}$ [km s^{-1}]
OIII	4363	–75	+45
OIII	4959	–80	+65
OIII	5007	–70	+60
OI	5577	–25	+25
OI	6300	–50	+40
OI	6364	–50	+30
SIII	6312	–60	+50
SII	4068	–25	+25
SII	4076	–50	+35
SII	6716	–50	+30
SII	6731	–50	+35
NII	5755	–70	+20
NII	6548	–70	+45
NII	6584	–80	+50
FeII	7155	–40	+30
ClIII	5517	–30	+100
ClIII	5538	–50	+40
Hα	6563	–1800	+1800
Hβ	4861	–160	+160
Hγ	4340	–140	+140
Hδ	4101	–100	+100
Hϵ	3970	–100	+100
H8	3889	–100	+40

region of the circumstellar material. In addition, the dispersion and signal-to-noise ratio of the spectra are different, which makes it difficult to compare individual lines. The question of line variability can thus only be answered by subsequent observations with identical setups, and differences between the Guerrero et al. (2001) spectrum and our data should not be

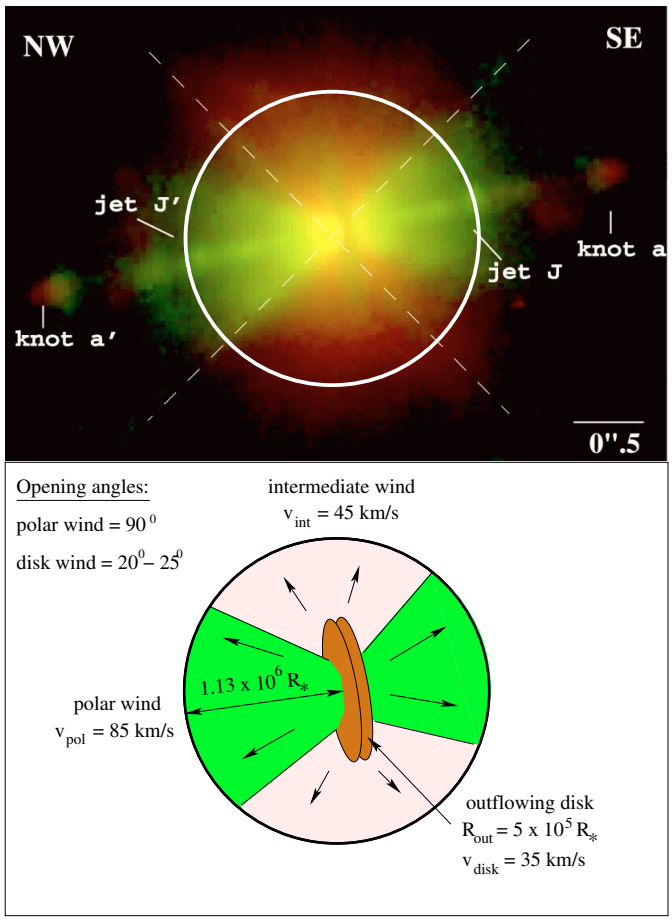

Fig. 7. *Top panel*: HST image of Hen 2-90 replotted with kind permission from Sahai et al. (2002). Overplotted is a big circle that indicates the width of the slit (which is 2″, corresponding to 0.019 pc at a distance of 2 kpc) of our Cassegrain observations from which the line luminosities have been derived. *Bottom panel*: Sketch of the threefold wind derived from the HST image and used in our calculations. Plotted are the outflowing disk, the polar wind, and the intermediate wind. Indicated are also the opening angles of the polar and disk wind used for the model calculations, and the velocities within the different wind regions as derived from Table 1 and discussed in the text. The whole structure is still embedded in an HII region that extends up to 3.″2 corresponding to 0.031 pc, which is 1.6 times larger than the non-spherical wind structure. The bipolar jet and the knots are not taken into account in the non-spherical wind model.

interpreted as source variability. What we can conclude, however, is that the circumstellar medium around Hen 2-90 is not homogeneous. On the contrary, the huge zoo of observed emission lines gives us a clear hint that the circumstellar medium must have a rather complex structure in both density and temperature, as indicated by the variety of line profiles, velocities, and ionization states.

4. The nature of the circumstellar material: nebula or wind?

In this section we discuss the nature of the circumstellar material close to the central star, whether it can be described by the nebula approximation often used for the analysis of planetary

nebula spectra or whether we have to apply a wind scenario. This discussion is based on the available observations: our optical spectra in combination with the HST image published by Sahai et al. (2002, see top panel of Fig. 7).

Emission lines: we observe from the innermost regions in Hen 2-90 permitted emission lines, as well as forbidden emission lines. The huge amount of forbidden lines might speak in favour of a nebula nature of the emitting material. However, we cannot explain the evenly huge amount of permitted lines with the nebula approximation because both sorts of lines need completely different density conditions: permitted lines are produced in regions of high density, forbidden lines are produced in regions of low density. The fact that both types of lines are very prominent in our spectra indicates that we need at least two different regions, one with high and one with low density. This might be consistent with the picture of a high density (ring?) nebula in the equatorial region and a low density nebula in polar region.

Ionization structure: inspection of the HST image (Fig. 7) shows clearly high-ionized material in the polar direction (= jet direction in the image), i.e. in the presumably low-density region, dominated by emission of [OIII], and low-ionized material at more intermediate latitudes (counted from the pole), dominated by [NII] emission. In our spectra, we found many forbidden emission lines as listed in Table 4. These lines are from ions in different ionization states and must therefore arise in regions of different ionization and, therefore, different temperature, consistent with the HST image. In addition, we found very strong emission of [OI], which means that this emission region must be neutral, also in hydrogen. The emission of the [OI] lines therefore must arise in (i) a (hydrogen) neutral region, speaking for high density material, at least close to the star, which guarantees shielding from the ionizing stellar flux, and (ii) in a medium of low density for the forbidden lines to be strong. The best location is the equatorial neutral disk-like structure visible in the HST image.

Velocity structure: our high-resolution spectra allow us also to derive the velocities from individual line profiles (see Table 1). We find that forbidden lines of different ionization stages, which can be connected with the different ionization regions seen in the HST image, have different velocities. The high-ionized lines thereby have the highest velocities, while the [OI] lines have the lowest.

The combination of all these results i.e. – (i) the coexistence of high- and low-density regions; (ii) a latitudal velocity structure having highest values in polar and lowest values in equatorial directions; (iii) a latitude-dependent ionization structure of the circumstellar material which also infers a latitudal temperature structure; and (iv) the variety of line profiles described in the previous section – seems to be more consistent with a non-spherical stellar wind scenario than with a simple constant density nebula scenario or even a piece-wise constant density nebula approximation. This conclusion was drawn solely from qualitative analysis of our observations in combination with the information that follows from the HST image. As we show in Sect. 5.3 when modeling the line luminosities of the forbidden emission lines, it turns out that saturation of the line luminosities happens for different lines at different distances from the star. This means that the forbidden lines are very sensitive to the density structure, supporting the idea of a radial density distribution rather than a constant density.

5. Modeling of the non-spherical wind

In the previous sections we have shown that the optical spectrum of Hen 2-90 contains many forbidden and permitted emission lines. Here we analyse some of the forbidden emission lines to derive the physical parameters of the emitting gas, such as electron temperature and density distribution, mass loss rate of the star, and the ionization structure of the circumstellar nebula. The stellar parameters of Hen 2-90 given by Costa et al. (1993) were derived using the spherically symmetric nebula approximation and are therefore relatively uncertain. Due to the lack of better parameter estimates we assume the star to be at a mean distance of 2 kpc for our model calculations, having an effective temperature of about 50 000 K and a radius of $0.38\,R_\odot$ (Kaler & Jacoby 1991; Costa et al. 1993).

5.1. Wind geometry

Based on the HST image of Sahai et al. (2002, see Fig. 7) we can distinguish three major wind regions: (i) a biconical high-ionization ([OIII] dominated) polar wind; (ii) a low-ionization ([NII] dominated) wind at intermediate latitudes, which we will call the intermediate wind; and (iii) an equatorial outflowing disk. The big white circle indicates the slit width of 2″ of our Cassegrain observations (the flux observed comes from this region). This corresponds to an outer edge of about 0.01 pc at a distance of 2 kpc. The HST resolved structure is embedded into a much larger HII region with extensions of at least $3\farcs2 \times 3\farcs1$ (Tylenda et al. 2003). Our observations therefore contain neither contribution from this extended nebula nor from the jets and knots, but are concentrated on the innermost non-spherical wind structure.

The HST image also hints at the location of the different ions. In combination with the velocity information retrieved from the line profiles (Table 1) we can determine the terminal wind velocities of the different regions. For the polar wind we find a mean velocity of $\sim 60\,\mathrm{km\,s^{-1}}$ from the [OIII] and [ClIII] lines. Taking the opening angle of the cone into account, which is about 90°, along with the fact that the system is seen (almost perfectly) edge-on, results in a terminal velocity of $\sim 85\,\mathrm{km\,s^{-1}}$. For the intermediate wind where the [SIII], [SII], and [NII] lines come from, we analogously derive a mean wind velocity of $\sim 45\,\mathrm{km\,s^{-1}}$; and for the disk wind, represented by the [OI] lines, we find a mean velocity of about $35\,\mathrm{km\,s^{-1}}$. The wind velocity shows a latitude dependence highest in the polar directions and lowest in equatorial direction, and the difference is a factor of ∼2.5.

With the adopted distance of 2 kpc we can derive linear scales for the different wind regions from the HST image. The polar wind is visible up to a distance of about $1.5 \times 10^6\,R_*$ which is slightly beyond our observing slit, which only extends to about $1.13 \times 10^6\,R_* \simeq 0.01$ pc. The outer edge of the disk is about $5 \times 10^5\,R_*$ and we estimate a total opening angle of 20−25°, based on the dark disk-like structure seen on the

HST image. The remaining volume is filled by the intermediate wind, which also shows indication of a high degree of ionization ([OIII] dominated) at its innermost parts. We estimate that this region extends roughly to about $r_{\rm out}(\rm OIII) \simeq 10^5\,R_*$.

5.2. The forbidden emission line luminosities

We concentrate our detailed analysis on the forbidden lines, which are excellent indicators of the circumstellar material for two reasons:

(i) They are excited collisionally, so are very sensitive to density and temperature;
(ii) The circumstellar nebula is optically thin for these lines, simplifying the analysis.

We model the line luminosities of the forbidden emission lines of OI, OII, OIII, NII, ClII, ClIII, ArIII, SII, and SIII in our spectra (see Table 4). We also find lines from CrII and CrIV, which we could not model due to the lack of collision parameters, and lots of FeII lines, which we also neglect because FeII cannot be treated in such an easy way as the other ions.

The line luminosity of a forbidden line is given by

$$L_\nu = \int j_\nu (1 - W(r)) \mathrm{d}V \tag{1}$$

where $j_\nu = h\nu N_{\rm i} A_{\rm ij}$ is the line emissivity and $W(r) = \frac{1}{2}(1 - \sqrt{1-(R_*/r)^2})$ is the geometrical dilution factor that accounts for the fraction of photons being intercepted by the star. For the line emissivity we need to calculate the level population. This is done for all the elements cited above by solving the statistical equilibrium equations in a 5-level atom. The collision parameters are taken from Mendoza (1983) and the atomic parameters from Wiese et al. (1966, 1969).

The hydrogen density in a wind follows from the mass continuity equation

$$N_{\rm H}(r) = \frac{\dot{M}}{4\pi r^2 \mu m_{\rm H} v(r)}. \tag{2}$$

$\dot{M}$ is the mass loss rate of the star and $v(r)$ the wind velocity, which is given by a β-law of the form

$$v(r) = v_\infty \left(1 - \frac{r_0}{r}\right)^\beta \tag{3}$$

with

$$r_0 = R_* \left\{1 - \left(\frac{v_0}{v_\infty}\right)^{\frac{1}{\beta}}\right\} \tag{4}$$

which sets the velocity at R_* equal to the sound velocity (v_0). v_∞ is the terminal velocity in each wind region which has been derived above from the different forbidden lines, and we set $\beta = 1$, which is a good approximation for winds of hot stars (Lamers & Cassinelli 1999).

The electron density is given in terms of the hydrogen density and depends on the degree of ionization in each part of the wind; in polar direction and in the inner parts of the intermediate wind we set $N_{\rm e} \simeq 1.1\,N_{\rm H}$. In these regions helium is singly ionized contributing about 10% to the total electron density. The contribution from other elements, like O, S, N, which are also (partly twice) ionized, to the total electron density is, however, negligible. For the outer parts of the intermediate wind, where He is assumed to be neutral, we use $N_{\rm e} \simeq 1.0\,N_{\rm H}$ (and again neglect the small contribution from the metals). For the disk wind where we assume that hydrogen is neutral, we have only electrons from elements with much lower ionization potential (i.e. lower than about 10 eV). Summing up the number densities of all these elements (assuming solar abundances), results in a maximum electron density in the disk of about $1.3 \times 10^{-4}\,N_{\rm H}$. As we cannot expect that all possible elements are completely ionized, we use an electron density of $N_{\rm e} \simeq 10^{-4}\,N_{\rm H}$, which is an *upper limit* to the real disk electron density. Since the excitation of the forbidden lines depends on the electron density, the fitting of the disk lines therefore results in a *lower limit* of the mass flux, i.e. the disk mass loss rate, because a decrease in electron density needs an increase in total density to account for the observed line luminosities.

For the temperature distribution we make use of the following equation

$$T(r) = T_\infty + (T_0 - T_\infty)\left(\frac{r}{R_*}\right)^{-x}. \tag{5}$$

Such a temperature distribution has been found to be a reasonable approximation for a wind of a hot star in radiative equilibrium by de Koter (1993). We set $x = 1$, but the value of x does not really influence the results because the forbidden lines are formed in the lower density region, far away from the star, where the temperature has already dropped to its terminal value, T_∞ (see Fig. 8). The line luminosities are, however, very sensitive to this terminal temperature.

One additional parameter that needs to be specified is the elemental abundance. Costa et al. (1993) have found that the elements are slightly sub-solar in Hen 2-90. However, these values have been derived under the assumption of a spherically symmetric homogeneous nebula, which is far from being the case. In addition, Kraus (2005) shows that the abundances can be much higher when derived using a stellar wind rather than a homogeneous nebula. We therefore start our calculations by assuming solar abundances (taken from Grevesse & Sauval 1998) for all elements. Deviations in the calculated line luminosities compared with observations might then be due to individual deviations in the abundances.

5.3. Mass fluxes and total mass loss rate

The results for the ions that are used to restrict the different parameters in our simple, non-spherical wind model are shown in Figs. 9–12, where we plotted the line luminosities as a function of r, i.e. the volume integrated flux that is achieved in the corresponding wind (i.e. polar, intermediate or outflowing disk) as it would be observed from such a wind with outer edge r. For several ions, the observed line luminosities do not come from only one of the three defined winds, but from two different wind regions. Therefore we briefly describe the procedure of how we fitted the different lines.

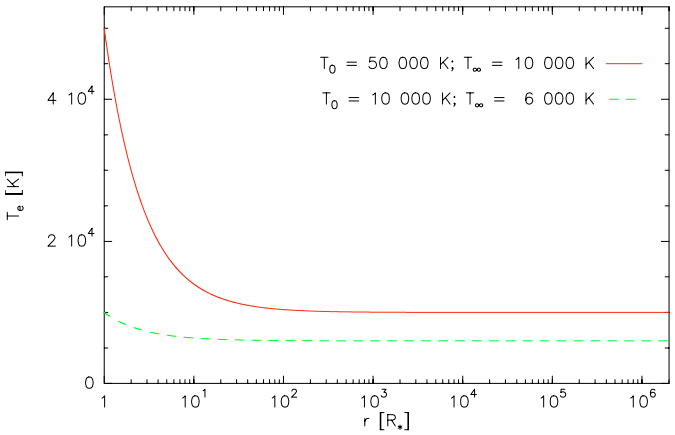

Fig. 8. Temperature distribution in the wind according to Eq. (5). The starting values T_0 and terminal values T_∞ appropriate for the polar/intermediate wind and for the outflowing disk are indicated. The temperature drops quickly (within 100 R_*) to its terminal value, which is found to be about 10 000 K in the polar and the intermediate wind and about 6000 K in the disk wind (see Table 2).

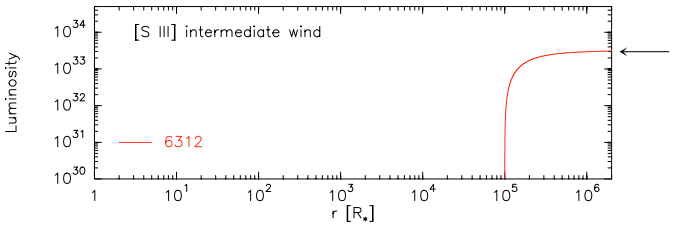

Fig. 9. Model results for the [SIII] line arising in the outer parts of the intermediate wind. Shown is the increase in line luminosity with distance from the star. The arrow on the right side of the panel indicates the observed value.

We started our modeling with the [SIII] 6312 Å line (Fig. 9). Since SIII and OII have about the same ionization potential, it can be expected that no SIII emission will come from regions of OIII emission. SIII emission is therefore restricted to the intermediate wind at distances from the star where OIII, and hence SIV, have recombined already. Therefore, the inner edge of the SIII emission is the outer edge of the OIII emission, i.e. $r_{\rm in}$(SIII) = $r_{\rm out}$(OIII) = $10^5\,R_*$ as found in Sect. 5.1.

The only free parameters are the temperature distribution and the mass loss rate at these intermediate latitudes. Since the SIII emission region is already rather far away from the star, we assumed the temperature to be constant and found a good fit for $T_{\rm e} \simeq 10\,000$ K. The mass flux of the intermediate wind has been found to be on the order of $F_{\rm m,int} = 1.5 \times 10^{-1}\,{\rm g\,s^{-1}\,cm^{-2}} = 1.66 \times 10^{-6}\,M_\odot\,{\rm yr^{-1}}$ steradian^{-1}.

Since SIII has only one prominent forbidden line in our spectral region, this best-fit temperature had to be confirmed with the other forbidden lines from the same wind region. Other elements like NII, SII, and ClII have more than one forbidden line, and several line ratios can be used as tracers for the electron temperature. From combining the results from all these temperature indicators, the best solution was found to be on the order of 10 000 K. The valid range of temperatures is very small, and the resulting uncertainty in mass flux is on the order of 20%. We want to stress that the dependence of the mass flux on electron temperature cannot be described with a power law, because the collision parameters have a more complicated temperature dependence.

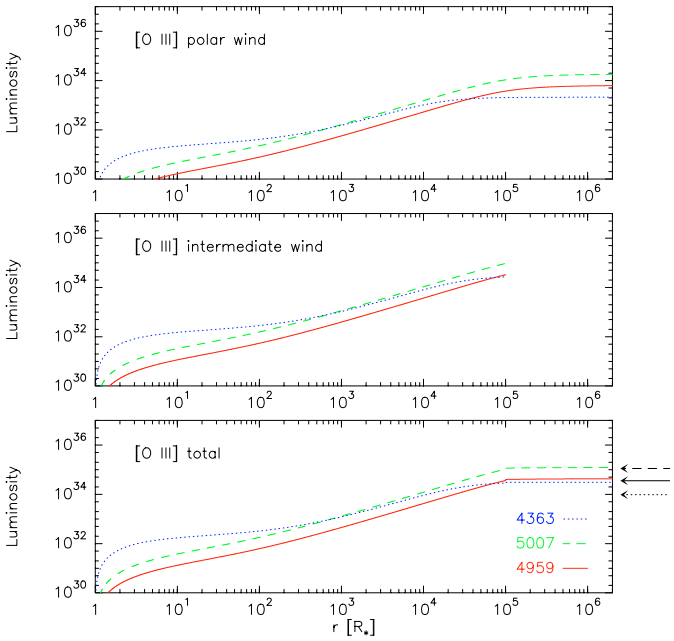

Fig. 10. Model results for the different [OIII] lines listed in the bottom panel. Shown are individual contributions from the polar and intermediate wind and their increase in line luminosity with distance from the star. The bottom panel shows the sum of both contributions, and the arrows on the right side indicate the observed value for each emission line (same line style).

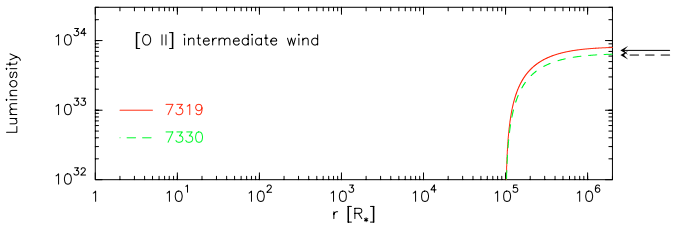

Fig. 11. Model results for the [OII] lines. These lines come from the intermediate wind only and from distances where OIII has already recombined (see mid-panel of Fig. 10). The arrows on the right side indicate the observed value for each emission line (same line style).

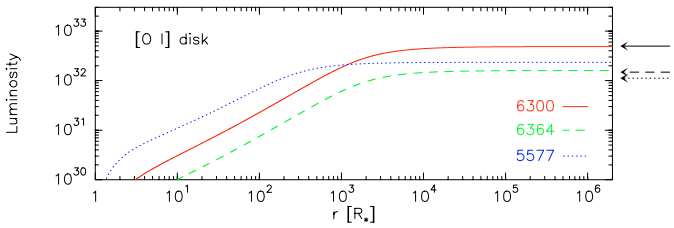

Fig. 12. Model results for the [OI] lines. These lines come from the disk wind only. The arrows on the right side indicate the observed value for each emission line (same line style).

The next element to fit is oxygen, so we started with the lines of OIII. These lines are supposed to come from 2 different regions (see Figs. 7 and 10): the inner parts of the intermediate wind and the polar wind. To get self-consistent results for all

Table 2. Best fit model parameters for the polar (p), intermediate (i), and disk wind (d). The mass fluxes are assumed to be constant within the indicated θ-ranges and have an error on the order of 20%.

	T_0	T_∞	$\theta_{\rm min}$	$\theta_{\rm max}$	v_∞	$F_{\rm m}(\theta)$
	[K]	[K]	[°]	[°]	[km s^{-1}]	[g s^{-1} cm^{-2}]
p	50 000	10 000	0	45	85	7.2×10^{-2}
i	50 000	10 000	45	78	45	1.5×10^{-1}
d	10 000	6000	78	90	35	5.5×10^{-1}

oxygen lines of different ionization state (Figs. 11 and 12), we had to decrease the O abundance from solar to 0.3 solar.

Contribution of the intermediate wind to the [OIII] lines is restricted to distances within $r_{\rm out}$(OIII). For the temperature distribution we used $T_0 = T_{\rm eff}$ and $T_\infty = 10\,000$ K. Using the effective stellar temperature as the starting temperature is quite reasonable because the star is supposed to be small, which means that the surface temperature is about equal to the effective temperature. In fact, the choice of the starting temperature does not really affect the behaviour of the line luminosities because the majority of the luminosity comes from the lower density regions where the temperature has reached its terminal value.

Once we have the contribution from the intermediate wind, the remaining line luminosities to the [OIII] lines must come from the polar wind. Here, the free parameters are again the mass flux and the temperature distribution. We found the best agreement by using the same temperature distribution as for the intermediate wind and a polar mass flux of $F_{\rm m,pol} = 7.2 \times 10^{-2}$ g s^{-1} cm^{-2} $= 7.99 \times 10^{-7}\,M_\odot$ yr^{-1} steradian^{-1}.

With these fixed parameters for the intermediate wind, we found good agreement between observed and modelled [OII] lines (Fig. 11). The remaining O lines are the [OI] lines, which are assumed to arise in the cool and neutral equatorial disk (Fig. 12). The only constraint on the modeling is the temperature distribution, which should start with a surface temperature around 10 000 K to guarantee that H is neutral. The terminal temperature, as well as the disk mass flux, could then be fixed by the best fit model (see Fig. 12) to $T_\infty = 6000$ K and $F_{\rm m,disk} = 5.5 \times 10^{-1}$ g s^{-1} cm^{-2} $= 6.10 \times 10^{-6}\,M_\odot$ yr^{-1} steradian^{-1}.

All the parameters for the three different wind regions are now fixed and summarised in Table 2. If this picture of the non-spherical wind is about correct, we should be able to fit the luminosities of the remaining forbidden lines (i.e. from SII, ClII, ClIII, ArIII, and NII) with the same sets of parameters.

The modeling of the [SII] lines was rather tricky, because they arise in two different regions: the hydrogen neutral disk and the outer parts of the (ionized) intermediate wind, but with no clear boundary conditions. For the intermediate wind, SII can only arise if SIII has recombined. Saturation of the [SIII] line luminosities happens at about $10^6\,R_*$ (Fig. 9), which is set as the minimum distance for the [SII] lines. For emission from the disk the inner edge is set to the stellar surface. A reliable fit is found from the simultaneous fitting of both contributions where we found that the disk contributes less than half to the total emission and that SII has to recombine at a distance of about $6000\,R_*$. Contribution from the intermediate wind, which is more than half of the total line luminosities, comes from a very narrow (in radius) region, starting at a distance of about $1.05 \times 10^6\,R_*$ just beyond the region of SIII line luminosity saturation and extending to the edge of our slit, which is at $1.13 \times 10^6\,R_*$. Since the line luminosities from the intermediate wind did not saturate at the outer edge of our slit, we expect the [SII] lines would appear much more luminous when observed with a larger slit width.

The predicted line luminosities of the nitrogen lines were much too high, so that we had to reduce the N abundance to 0.5× solar to achieve good fits.

In Table 3 we summarise all the observed (Col. 3) and modelled (Col. 4) line luminosities, as well as the ratio of observed over modelled luminosity (Col. 5) and the location(s) of the ions in either the polar wind (p), intermediate wind (i) or disk (d) alone, or a combination of two of them. We thereby distinguish two sets of lines: (1) those which are used to derive

Table 3. Observed and modelled forbidden line luminosities. For the observed values, we took the intensities given in Table 4 and assumed a distance of 2 kpc. The fifth column contains the ratio of observed over modelled line luminosity, and in the sixth column we describe in which part(s) of the wind the line is produced. The classifications of p, i, and d mean polar wind, intermediate wind, and disk, respectively. In the upper part we gathered the lines used to derive the mass fluxes and temperature distributions in each wind zone, while the lines in the lower part have been used to confirm the models and to derive the abundance, especially in the case of N.

Ion	λ (Å)	$L_\lambda^{\rm obs}$	$L_\lambda^{\rm model}$	ratio	region
OIII	4363	9.71×10^{33}	2.90×10^{34}	0.33	p,i
OIII	4959	3.58×10^{34}	3.91×10^{34}	0.92	p,i
OIII	5007	1.13×10^{35}	1.13×10^{35}	1.00	p,i
OII	7319	7.23×10^{33}	7.70×10^{33}	0.94	i
OII	7330	6.18×10^{33}	6.17×10^{33}	1.00	i
OI	5577	1.12×10^{32}	2.33×10^{32}	0.48	d
OI	6300	4.98×10^{32}	4.86×10^{32}	1.02	d
OI	6364	1.49×10^{32}	1.60×10^{32}	0.93	d
SIII	6312	2.95×10^{33}	2.98×10^{33}	0.99	i
SII	4068	1.15×10^{33}	4.57×10^{32}	2.52	i,d
SII	4076	3.43×10^{32}	1.18×10^{32}	2.90	i,d
SII	6716	9.05×10^{31}	1.05×10^{32}	0.86	i,d
SII	6731	2.13×10^{32}	2.20×10^{32}	0.97	i,d
NII	5755	4.56×10^{33}	4.57×10^{33}	1.00	i
NII	6548	4.84×10^{33}	6.15×10^{33}	0.79	i
NII	6584	2.08×10^{34}	1.81×10^{34}	1.15	i
ClIII	5517	1.10×10^{32}	4.23×10^{31}	2.60	p,i
ClIII	5538	1.74×10^{32}	1.74×10^{32}	1.00	p,i
ClII	6153	3.88×10^{31}	3.82×10^{31}	1.01	i
ArIII	5193	1.16×10^{32}	6.44×10^{32}	0.18	p,i
ArIII	7136	7.37×10^{33}	6.88×10^{33}	1.07	p,i
ArIII	7753	1.49×10^{33}	1.68×10^{33}	0.89	p,i

the mass fluxes and temperature distributions in the different wind regions are collected in the upper part, and (2) the lines that are used for confirmation of the models and for derivation of the abundance (especially of N) are given in the lower part.

Inspecting Table 3 shows that some of the modelled lines can be off by a factor of 2 or larger. Here, we give some arguments that might explain these differences.

1. We start with the [OI] line at $\lambda = 5577$ Å, for which our model predicts about twice as much luminosity as observed. This line corresponds to the transition $5 \longrightarrow 4$ in our adopted 5-level atom. There exists one permitted transition between its upper level and a much higher level with wavelength $\lambda = 1217.6$ Å, which falls into the wavelength range covered by a broadened Ly α line ($\lambda_{\mathrm{Ly}\,\alpha} = 1215.6$ Å). The fifth level might therefore be depopulated radiatively into this higher state from which several permitted lines arise, and the observable 5577 Å line luminosity will decrease.
2. An important source of error might be the foreground extinction used to de-redden our data. We took the foreground extinction value from Costa et al. (1993), who derive it from the Balmer lines, which they assumed to arise in a spherically symmetric constant density nebula. Since some of the modelled line luminosities arising in the blue part of the spectrum (at $\lambda < 5000$ Å) are off compared to the observed luminosities, it seems that this might be a systematical error rather than a model error. However, our modeling procedure is not suitable to derive the real extinction value. A slightly different extinction will certainly result in slightly different model parameters; e.g. the mass fluxes in the different wind regions will change individually. This makes it difficult to predict in what way the extinction might be off, especially since some of the forbidden lines arise in two different regions and have to be fitted simultaneously, as e.g. the [SII] lines. Nevertheless, de-reddening with the correct extinction value is especially important if we have to compare lines from the same ion arising in the very blue part of the spectrum with lines coming from the very red part of the spectrum, which is the case e.g. for the lines of ArIII where we have a deviation of the blue line with respect to the red lines by a factor of 5!
3. An additional reason for the deviations might be the accuracy of the measured line fluxes coming from different wavelength regions. As explained in Sect. 2, the line fluxes from the high and low wavelength regions, i.e. at wavelengths $\lambda < 5000$ Å and $\lambda > 7000$ Å, have much larger uncertainties due to the lower *S/N* ratio and efficiency of the CCD leading to larger errors in the measured line fluxes.

Except for the [OI] 5577 Å line we think that both effects, a slightly different foreground extinction, and a larger uncertainty in the measured line fluxes each play a role but it is difficult to disentangle the individual influence of these effects on a specific line.

From the results presented in Table 2 for the different wind parts, it is obvious that the mass flux varies with latitude being lowest at the poles and highest at the equator with $F_{\mathrm{m,disk}} \simeq 8\, F_{\mathrm{m,pole}}$. The total mass loss rate of the star is given by the integral of the mass flux over the stellar surface, which is

$$\dot{M} = 4\pi R_*^2 \int_0^{\pi/2} F_{\mathrm{m}}(\theta) \sin\theta \mathrm{d}\theta. \quad (6)$$

Inserting our values given in Table 2, we find a total mass loss rate of the star of $\dot{M} \simeq (2.9 \pm 0.6) \times 10^{-5}\, M_\odot\,\mathrm{yr}^{-1}$. The error results from the uncertainties in mass flux.

5.4. The wings of Hα

With this complete wind scenario derived in the previous section we can return to the question whether the broad wings of the Hα line are due to outflow or electron scattering. From our data we derive a contribution of about 10% of the broad wings to the total intensity, which implies an electron scattering optical depth of about 0.09 in and above the line formation region of Hα. On the other hand, we can calculate the electron optical depth from

$$\tau_{\mathrm{e}} = \int N_{\mathrm{e}}(r)\sigma_{\mathrm{e}} \mathrm{d}r \quad (7)$$

where $N_{\mathrm{e}}(r)$ is the electron density distribution in the line of sight between the observer and the formation region of the line, and σ_{e} is the electron scattering coefficient. Since we see Hen 2-90 more or less edge-on, we can use the electron density distribution from the intermediate wind and calculate backwards, i.e. from the observer into the wind, to determine where in the wind most of the Hα emission is produced. For our intermediate wind electron density distribution and the optical depth of 0.09 we find that the majority of the Hα emission arises within about $4000\,R_*$ around the star, which is the region of highest density and therefore the most plausible location. We can therefore state that the wings of Hα are indeed produced due to electron scattering and not due to a high velocity wind.

Additional confirmation of the broadening due to electron scattering rather than due to high velocity outflow is provided by the wind scenario proposed above. Our non-spherical wind model covers the complete surroundings of the star except for the highly-collimated jets, which have been found to have real outflow velocities of less than $400\,\mathrm{km\,s^{-1}}$ (see e.g. Sahai et al. 2002). What we found from our wing velocity measurements in all the different parts of the wind is: a terminal outflow velocity of (i) about $85\,\mathrm{km\,s^{-1}}$ from the [OIII] lines in the polar wind, (ii) about $40\,\mathrm{km\,s^{-1}}$ from the [NII] and [SIII] lines in the intermediate wind, and (iii) about $35\,\mathrm{km\,s^{-1}}$ from the [SII] and [OI] lines in the disk. We could not identify any additional wind component that might have an outflow velocity as high as $1800\,\mathrm{km\,s^{-1}}$.

6. Discussion

6.1. The non-spherical wind scenario for Hen 2-90

For the model calculations we use the geometry and ionization structure based on the HST image (Fig. 7), which clearly shows

a polar wind, an intermediate wind, and a disk so that the geometry used seems to be well justified.

Such a non-spherical wind model with latitude-dependent temperature, terminal wind velocity, and mass flux might be understood in terms of a rotating star. According to the van Zeipel theorem, rapid rotation will lead to polar brightening, which means that the surface temperature of the star can be much hotter on the pole compared to the equator. Our calculations show that in equatorial regions the surface temperature should not be higher than about 10 000 K to guarantee that hydrogen is neutral. In polar directions we found that the terminal temperature should not be lower than about 10 000 K, which means that the surface temperature can be much hotter. We do not have a good handle on the real polar surface temperature because the forbidden emission lines are produced far away from the star where the temperature has dropped already to its terminal value. In our calculations we used the effective temperature of 50 000 K found by Kaler & Jacoby (1991) with the Zanstra method. Cidale et al. (2001) derived a much lower effective temperature of only 32 000 K using the energy balance method. We tested our model for different polar surface temperatures in the range $T_0 = 15\,000-50\,000$ K and found that, for different surface temperatures, large differences occur in the line luminosities close to the star. However, in the regions of our interest, where the lines saturate, the line luminosities are all about equal. This implies that from our observations we cannot draw any conclusion about the real polar surface temperature.

Rotation not only influences the surface temperature structure, but also the terminal wind velocities resulting in a decrease in terminal velocity from pole to equator (see e.g. Lamers & Cassinelli 1999; Kraus & Lamers 2005). This is exactly what we found from our observations, when we take the known inclination of the system into account as suggested from the HST image.

The ratio of polar ($85\,\mathrm{km\,s^{-1}}$) to disk terminal velocity ($35\,\mathrm{km\,s^{-1}}$) of about 2.4, derived from the forbidden emission lines, is consistent with a rotation speed of about 75−80% of the critical velocity (Kraus & Lamers 2005). Such high velocities are observed e.g. for the classical Be stars (see e.g. Porter & Rivinius 2003). Some of those stars have recently been suggested as rotating even close to break-up, i.e. with almost critical velocity (Townsend et al. 2004).

An additional effect of rotation is that it leads to a latitude-dependent mass flux, which is also the case for Hen 2-90. A mechanism like the wind compressed disk (Bjorkman & Cassinelli 1993) or the rotation-induced bistability (Lamers & Pauldrach 1991), or a combination of both, can result in the observed high density equatorial outflowing disk.

This combination of the latitude-dependent mass flux and surface temperature also explains why we see different ionization structures at different latitudes. The lower surface temperature results in less ionizing UV photons, and the higher mass flux into a higher shielding density, which in the end reduces the degree of ionization.

For our model calculations the outflowing disk is assumed to be neutral in hydrogen. Kraus & Lamers (2003) showed that in the case of supergiants, the disk created by an equatorial wind can indeed become neutral just above the stellar surface, if the equatorial mass flux is high enough to prevent ionizing stellar photons from penetrating into the high density equatorial disk wind. Although Hen 2-90 is hotter than a typical supergiant (but its effective temperature might well be only 32 000 K instead of 50 000 K as stated above), it also has a much smaller radius leading to an enormous equatorial mass flux, whose material is indeed dense enough to shield the disk material efficiently from stellar irradiation. Consequently, the disk will stay neutral even close to the stellar surface.

The terminal temperature found for the gas disk is about 6000 K. From our modeling we found that the luminosities of the forbidden lines coming from the disk saturate at a distance of about $2 \times 10^4\,R_*$. The total size of the disk is, however, much larger, at least $5 \times 10^5\,R_*$. The ISO spectrum of Hen 2-90 shows strong IR excess emission due to hot circumstellar dust that can only be located in the disk. The evaporation temperature of dust is between 1500 K and 2000 K depending on its composition. In the temperature region between the atomic and the dust dominated regions, the atoms might be locked into molecules that can form (and survive) at temperatures below about 5000 K. Our results are therefore also consistent with a circumstellar dust disk where the dust forms far away from the star, at distances $r_{\rm dust} \gg 2 \times 10^4\,R_* \simeq 35$ AU. A detailed study of the ISO spectrum to calculate the infrared emission coming from the predicted dust disk is necessary and currently under investigation (Borges Fernandes & Lorenz-Martins, in preparation).

It would be interesting to see whether the ionization structure we found from our modeling of the forbidden emission lines might be reproduced by more sophisticated ionization structure calculations in such a non-spherically symmetric wind scenario. Unfortunately, as far as we know, no numerical codes exist that can perform the 3D radiation transfer needed for non-spherical ionization structure calculations.

Finally, we qualitatively discuss how the variety of the line profiles, as shown in Sect. 3, might be produced in our non-spherical wind scenario. Even though the central star might be rapidly rotating, we do not think that the double-peaked line profiles mirror the stellar rotation or are due to rotation at all (although we cannot ad hoc exclude a rotational contribution), because the effective temperature of about 50 000 K indicates that the star must have a line-driven wind. The acceleration of the wind to its terminal velocity happens within only a few stellar radii, leading to a radially outflowing wind.

Double-peaked lines: these lines are mainly produced in the intermediate wind (some of them with a Gaussian contribution from the polar wind), which can be regarded as a thick expanding torus. Since we see this torus edge-on, the emission lines formed within it show double-peaked profiles. Since the maximum (terminal) wind velocity of the intermediate wind is about $45\,\mathrm{km\,s^{-1}}$, the peak separation will be on the order of 40 to $50\,\mathrm{km\,s^{-1}}$, as observed.

Broad single-peaked lines: they are found for the hydrogen Balmer lines. As discussed already in Sect. 5.4, the broad wings of Hα are due to electron scattering with a scattered intensity of about 10%. With increasing quantum number, the Balmer line intensities decrease and a 10% contribution in the broad wings becomes much harder to detect above the

continuum. That's why with increasing quantum number the derived wing velocities of the Balmer lines decrease until they adapt to the terminal wind velocities derived from the forbidden lines (see e.g. line H8 in Table 1).

Narrow single-peaked lines: these lines are mainly formed in the disk, even though some of them can have small contributions from the intermediate wind. The lines formed in the outflowing edge-on seen disk should also show double-peaks as do the lines formed in the intermediate wind. However, since the disk outflow velocity is smaller than the velocity in the intermediate wind, the two peaks merge, leading to a single-peaked line profile.

The variety of profiles observed can be explained with our model assumptions. However, we have no explanation for those asymmetric line profiles with a strong red peak. Probably, our scenario is not completely correct, and effects like clumping in the wind might be worth investigating.

A quantitative analysis of the line profiles would be necessary, but this is difficult with our present data and beyond the scope of this paper, because the profiles are derived from the FEROS spectrum which is not flux calibrated, while the line luminosities have been derived from the low-resolution Cassegrain spectrum, which makes it impossible to model line luminosities and profiles simultaneously.

6.2. Hen 2-90: a symbiotic object or a compact planetary nebula?

In the literature Hen 2-90 has been classified either as a (compact) planetary nebula (e.g. Costa et al. 1993; Maciel 1993; Lamers et al. 1998) or as a symbiotic object, i.e. a binary consisting of a cool giant and a hot component with an accretion disk (Sahai & Nyman 2000; Guerrero et al. 2001).

The HST image (Fig. 7, Sahai et al. 2002) clearly shows the presence of a nebula bisected by a disk, with a highly collimated and bipolar jet with several pairs of knots on both sides. This scenario could be explained assuming that Hen 2-90 is either a compact planetary nebula, where the wind asymmetries started during the AGB phase, or a binary system, where the jets are caused by an accretion disk.

During our modelling procedure we found, as also cited by Costa et al. (1993) and Maciel (1993), a depletion of N and O by a factor of 2 and 3.3, respectively, with respect to the electron density with S, Ar, and Cl having normal (i.e. solar) abundances. In addition, the FEROS spectrum contains only one single permitted carbon line, CII λ6578. This line has previously been detected by Costa et al. (1993) and Guerrero et al. (2001), but it is very weak in the FEROS spectrum (just at the detection limit) and absent in the Cassegrain spectrum. We can only estimate its line flux and we found about 0.06 for the observed flux and about 0.02 for the dereddened flux in the scaling of Table 4 (Hβ = 100). The uncertainty of these line fluxes is about 50%. No forbidden emission line of carbon was detected, even though in the optical spectrum we would expect to observe several [CI] lines coming from the disk. We applied our disk wind model to calculate the line luminosities for these carbon lines, and found that these lines would only show up in the spectrum for a carbon abundance of at least twice solar. Inspection of the ISO spectrum of Hen 2-90 reveals emission from oxygen-rich dust (Borges Fernandes & Lorenz-Martins, in preparation). This dust can only be the dominant dust component in the case O/C > 1 during the ejection time of the dust-forming material. We found an underabundance of O by more than a factor of 3. Together with the fact that the dust composition should mirror the actual wind composition (unless the star has changed its composition from O-rich to C-rich since the ejection of the dust forming material, which is rather unlikely), we conclude that (i) the progenitor star that ejected the dust forming material cannot have been carbon rich, and (ii) the actual carbon abundance must be less than 0.6 solar to guarantee O/C > 1. Assuming a standard scenario with dredge-ups, we can understand the depletion of C and O; however, we have no explanation for the fact that N is also depleted. There are some *B-type* post-AGB stars in the halo of our Galaxy which also show this behaviour (Moehler & Heber 1998), and recently Lennon et al. (2005) reported on a Be star with an unexpected low N abundance. However, the origin of those anomalies is still poorly understood. Rotation or a possible binarity could play an important role. Unfortunately, as far as we know, no stellar evolution models exist that follow the whole life sequence of rapidly rotating intermediate mass stars, for which Hen 2-90 seems to be a candidate.

Another point that should be noted is that from our spectra, which cover the complete optical wavelength range, we have identified no lines from ions with ionization potential higher than ~40 eV and consequently no He II lines. In addition, there is no indication for the presence of TiO bands either. These two characteristics are the main signature of a symbiotic system. Since we see the disk of Hen 2-90 almost edge-on, it might be possible that the disk hides the atmosphere of a cool giant, where the TiO bands are formed, and also absorbs the He II emission from a hot component. However, the fact that we don't see hints for any other line from ions with ionization potential higher than ~40 eV leads us to the conclusion that these ions (and therefore also He II) do not exist in the wind of Hen 2-90 indicating that (i) the effective temperature of Hen 2-90 is indeed much lower than the 50 000 K found from the Zanstra method and may well be around 32 000 K as derived by Cidale et al. (2001) from the energy balance, and (ii) the symbiotic system is not the favoured classification.

Besides the absence of clear indications for a classification as a symbiotic object, our results favour the conclusion of Hen 2-90 being a compact planetary nebula and two more features support this idea:

1. The mass loss rate of $\sim 3\times10^{-5}\,M_{\odot}\,\mathrm{yr}^{-1}$ found for Hen 2-90 coincides with those found for proto-planetary nebulae with axially symmetric dust shells resulting from a so-called superwind (see e.g. Meixner et al. 1997).
2. An observational curiosity in the spectrum of Hen 2-90 is the fact that the [OIII] 5007 Å line is less intense than the Hα line, although for a compact planetary nebula, it is usually the other way round. However, in our forbidden line analysis, we found that the abundance of O had to be reduced to only 0.3 solar to achieve reasonable line

luminosity fits. This means that, if Hen 2-90 had a "normal" O abundance, the 5007 Å line would be about 3.3 times stronger than observed, and consequently be higher than the Hα flux. The anomalous line flux is therefore due to the underabundance of O.

We cannot definitely exclude a binary nature for Hen 2-90 (see also the discussion in Kraus et al. 2005). Unfortunately, the optical continuum of Hen 2-90 is completely flat, making it impossible to disentangle individual components. In addition, the optical continuum is mainly due to free-free and free-bound emission in the optically thick wind, rather than due to the stellar continuum.

Observed features that might hint at a binary nature are the jet-like structure with blob ejections (Sahai 2002; Sahai et al. 2002) and the DENIS NIR photometry cited by Guerrero et al. (2001):

Jet-like structure and blob ejection: the jet structure seen in Hen 2-90 is very collimated, and the blobs are found to be ejected regularly on a 40-year timescale. This perfect alignment of the jet axis and the blobs is unique. All PNe that are known to be binaries show either asymmetric or point-symmetric jet and blob ejection. In addition, to date no X-ray emission coming from an accretion disk has been detected from the system, which might indicate a completely different formation mechanism. García-Segura et al. (2001) modeled the jet and knots of Hen 2-90 using the concept of magnetohydrodynamics in the wind of a single star and under the assumption of a solar-like magnetic cycle. This model does not need a binary for jet production, because the jet formation is not driven by an accretion disk. A binary component might be helpful in the first instance to spin-up the star to high rotation rates (e.g. in a merger process) and, therefore, to increase the stellar magnetic field to the values needed for their model calculations. Such a spin-up might also explain the high rotation velocity of the central star which we claimed in the previous section and derived from the observed terminal velocities.

DENIS NIR photometry: Schmeja & Kimeswenger (2001) used the new DENIS survey data to probe different types of PNe. Their Fig. 1 shows a distinction between genuine PNe, symbiotic Miras, and IR-[WC] PNe on the basis of a colour-colour plot. With the published DENIS photometry data of Hen 2-90 (Schmeja & Kimeswenger 2002), and corrected for the extinction value of Costa et al. (1993), Hen 2-90 falls into the intermediate region between the genuine PNe and the IR-[WC] PNe. However, the IR-[WC] PNe are supposed to have strong PAH emission, which increases their K-band flux and shifts them off the genuine PNe region. A pollution of the K-band emission might also be present for Hen 2-90, which shows a huge zoo of emission features in the IR. Subtraction of this polluting emission might shift Hen 2-90 back into the regime of the genuine PNe. In addition, the carbon abundance found for Hen 2-90 is much too small to classify it as a carbon rich star.

From our observations, modeling, and the above discussion, we conclude that Hen 2-90 must be at least an evolved and probably rapidly rotating object, and the classification as a compact planetary nebula seems to be favourable. The question whether this compact planetary nebula is part of a binary system can only be solved if clear direct indications of a companion star are observed, which is up to now not the case but makes it worth looking at this object in much more detail.

7. Conclusions

In this paper we studied the non-spherical mass loss history of Hen 2-90 by splitting the analysis into a qualitative and a quantitative part. In the first part, we presented high and low resolution optical observations of the innermost non-spherical wind structure around Hen 2-90. The spectra contain a huge number of forbidden and permitted emission lines of different ionization states justifying the classification of Hen 2-90 as an object showing the B[e] phenomenon. The emission lines can be separated into four groups according to the different shape of their profiles: broad and narrow single-peaked lines, double-peaked lines, and lines with a well pronounced shoulder. This variety of line profiles indicates a complex structure of the circumstellar medium. There are no absorption lines present in the spectrum.

In the second part of the paper we performed a detailed analysis of the forbidden emission lines. The wind geometry used is based on the HST image, which reveals a non-spherical wind structure consisting of a polar wind, an outflowing disk, and an intermediate wind in between them (see Fig. 7). In all three parts, the ionization structure is different, indicating a latitude dependence of the surface temperature and the mass flux. These assumptions could be confirmed by our forbidden line analysis and might be interpreted in terms of a rapidly rotating (75−80% critical) underlying star. We could determine mass fluxes of $0.07 \pm 0.01\,\mathrm{g\,s^{-1}\ cm^{-2}}$, $0.15 \pm 0.03\,\mathrm{g\,s^{-1}cm^{-2}}$, and $0.55 \pm 0.11\,\mathrm{g\,s^{-1}\,cm^{-2}}$ (i.e. $7.99 \times 10^{-7}\,M_\odot\,\mathrm{yr^{-1}\ steradian^{-1}}$, $1.66 \times 10^{-6}\,M_\odot\,\mathrm{yr^{-1}\ steradian^{-1}}$, and $6.10 \times 10^{-6}\,M_\odot\,\mathrm{yr^{-1}\ steradian^{-1}}$) for the polar, intermediate, and disk wind, respectively. The surface temperature might change from 50 000 K−32 000 K (or less) at the pole to about 10 000 K at the equator, and the terminal velocities are $85\,\mathrm{km\,s^{-1}}$ (polar wind), $45\,\mathrm{km\,s^{-1}}$ (intermediate wind) and $35\,\mathrm{km\,s^{-1}}$ (disk). The total mass loss rate was found to be $(2.9 \pm 0.6) \times 10^{-5}\,M_\odot\,\mathrm{yr^{-1}}$.

From the near absence of observable carbon lines in our spectra and from the fact that Hen 2-90 clearly shows O-rich dust in the ISO spectrum, we could restrict the C abundance to a value less than about 0.6 solar. In addition we found that the O abundance is 0.3 solar and the N abundance is about 0.5 solar leading to an enhanced N/O ratio of 5/3 with respect to the solar value, while Ar, S, and Cl could be modelled with solar abundances. The depletion of C and O follow from stellar evolution, but for the depletion of N we have no satisfying explanation, as it cannot be explained by a standard stellar evolution scenario with dredge-ups.

From our observations and modeling results we conclude that Hen 2-90 must be an evolved object with most probably a rapidly rotating central star, and we favour the interpretation of Hen 2-90 as a compact planetary nebula. Whether it is part of a binary system is still an unsolved question. More observations and better evolutionary models for rapidly rotating stars

are certainly needed for better comprehension of this very curious object.

Acknowledgements. We would like to thank the anonymous referees for remarks and suggestions that have led to a significant improvement of this paper. M.K. also thanks Guillermo García-Segura for helpful discussions on PNe. M.K. was supported by the German *Deutsche Forschungsgemeinschaft, DFG* grant number Kr 2163/2–1 and by the Nederlandse Organisatie voor Wetenschappelijk Onderzoek (NWO) grant No. 614.000.310. M.B.F. acknowledges financial support from *CAPES* (Ph.D. scholarship). M.B.F. also acknowledges Utrecht University for the warm hospitality during his one-year stay there.

References

Bjorkman, J. E., & Cassinelli, J. P. 1993, ApJ, 409, 429
Cidale, L., Zorec, J., & Tringaniello, L. 2001, A&A, 368, 160
Costa, R. D. D., de Freitas Pacheco, J. A., & Maciel, W. J. 1993, A&A, 276, 184
de Koter, A. 1993, Studies of the Variability of Luminous Blue Variable Stars, Ph.D. Thesis, Utrecht, The Netherlands
García-Segura, G., López, J. A., & Franco, J. 2001, ApJ, 560, 928
Grevesse, N., & Sauval, A. J. 1998, Space Sci. Rev., 85, 161
Guerrero, M. A., Miranda, L. F., Chu, Y. H., Rodriguez, M., & Williams, R. M. 2001, ApJ, 563, 883
Hamuy, M., Suntzeff, N. B., Heathcote, S. R., et al. 1994, PASP, 106, 566
Henize, K. G. 1967, ApJS, 14, 125
Imai, H., Obara, K., Diamond, P. J., Omodaka, T., & Sasao, T. 2002, Nature, 417, 829
Kaler, J. B., & Jacoby, G. H. 1991, ApJ, 372, 215
Kraus, M. 2005, in Planetary Nebulae beyond the Milky Way, ed. J. R. Walsh, & L. Stanghellini, ESO Astrophysics Symposia (Heidelberg: Springer) [arXiv:astro-ph/0407292]
Kraus, M., & Lamers, H. J. G. L. M. 2003, A&A, 405, 165
Kraus, M., & Lamers, H. J. G. L. M. 2005, in preparation
Kraus, M., Borges Fernandes, M., & de Araújo, F. X. 2005, in Massive Stars in Interacting Binaries, ed. A. Moffat, & N. St-Louis (San Francisco: ASP Conf. Ser.) [arXiv:astro-ph/0410196]
Kwok, S. 2000, The Origin and Evolution of Planetary Nebulae, 5, Cambridge Astrophys. Ser., 31
Lamers, H. J. G. L. M., & Cassinelli, J. P. 1999, Introduction to Stellar Winds (Cambridge University Press), 9
Lamers, H. J. G. L. M., & Pauldrach, A. W. A. 1991, A&A, 244, L5
Lamers, H. J. G. L. M., Zickgraf, F.-J., de Winter, D., Houziaux, L., & Zorec, J. 1998, A&A, 340, 117
Landaberry, S. J. C., Pereira, C. B., & de Araújo, F. X. 2001, A&A, 376, 917
Lennon, D. J., Lee, J.-K., Dufton, P. L., & Ryans, R. S. I. 2005, A&A, submitted [arXiv:astro-ph/0407258]
Maciel, W. J. 1993, Ap&SS, 209, 65
Meixner, M., Skinner, C. J., Graham, J. R., et al. 1997, ApJ, 482, 897
Mendoza, C. 1983, IAU Symp., 103, 143
Moehler, S., & Heber, U. 1998, A&A, 335, 985
Moore, C. E. 1945, A Multiplet Table of Astrophysical Interest, Part I – Table of Multiplets, Revised Ed. (Princeton, New Jersey: Princeton University Observatory)
Porter, J. M., & Rivinius, Th. 2003, PASP, 115, 1153
Sahai, R. 2002, Rev. Mex. Astron. Astrofis, 13, 133
Sahai, R., & Trauger, J. T. 1998, AJ, 116, 1357
Sahai, R., & Nyman, L.-A. 2000, ApJ, 537, L145
Sahai, R., Brillant, S., Livio, M., et al. 2002, ApJ, 573, L123
Schmeja, S., & Kimeswenger, S. 2001, A&A, 377, L18
Schmeja, S., & Kimeswenger, S. 2002, Hvar Obs. Bull., 26, 45
Thackeray, A. D. 1967, MNRAS, 135, 51
Townsend, R. H. D., Owocki, S. P., & Howarth, I. D. 2004, MNRAS, 350, 189
Tylenda, R., Siódmiak, N., Górny, S. K., Corradi, R. L. M., & Schwarz, H. E. 2003, A&A, 405, 627
Vinković, D., Elitzur, M., Hofmann, K.-H., & Weigelt, G. 2004, in Asymmetric Planetary Nebulae III, Vol. XXX, ed. M. Meixner, J. Kastner, B. Balick, & N. Soker, ASP Conf. Ser.
Webster, L. B. 1966, PASP, 78, 136
Wiese, W. L., Smith, M. W., & Glennon, B. M. 1966, Atomic Transition Probabilities, Vol. 1, National Standard Reference Data System, Washington DC
Wiese, W. L., Smith, M. W., & Miles, B. M. 1969, Atomic Transition Probabilities, Vol. 2, National Standard Reference Data System, Washington DC

Online Material

Table 4. Emission line intensities relative to Hβ = 100 obtained with B&C spectrograph.

Wavelength (Å)	$I_{obs}(\lambda)$	$I_{corr}(\lambda)$	Identification
3833.8	3.14	12.88	H9 3835.4
3867.1	1.67	6.37	He I (m20) 3867.5
3887.5	7.20	26.22	He I (m2) 3888.7
			H8 3889.1
3968.6	6.06	20.37	Hϵ 3970.1
4025.5	1.15	3.48	He I (m18) 4026.2
4068.0	0.95	1.78	S II [m1F] 4068.6
4075.8	0.33	0.53	S II [m1F] 4076.2
4101.4	11.24	33.26	Hδ 4101.7
4120.5	0.19	0.45	O II (m20) 4119.2
			O II (m20) 4120.3
			O II (m20) 4120.6
			He I (m16) 4121.0
			S II (m2) 4121.0
4143.8	0.30	0.85	He I (m53) 4143.8
4178.8	0.23	0.41	Fe II (m28) 4178.9
			Fe II [m21F] 4177.2
			Fe II [m23F] 4179.0
4233.4	0.12	0.17	Fe II (m27) 4233.2
4245.0	0.14	0.26	Fe II [m21F] 4244.8
4288.0	0.20	0.38	Fe II [m7F] 4287.4
4341.3	24.40	54.89	Hγ 4340.5
4364.0	4.12	15.03	O III [m2F] 4363.2
4388.6	0.51	0.99	He I (m51) 4387.9
4416.3	0.46	0.83	Fe II (m27) 4416.8
			Fe II [m6F] 4414.5
			Fe II [m6F] 4416.3
4472.7	3.68	6.68	He I (m14) 4471.7
4490.9	0.08	0.21	Fe II [m6F] 4488.8
			Fe II (m37) 4491.4
4520.8	0.26	0.36	Fe II (m37) 4520.2
			Fe II (m38) 4522.6
4554.3	0.23	0.38	S III (m2) 4552.7
4584.7	0.22	0.33	Fe II (m37) 4582.8
			Fe II (m38) 4583.8
			Fe II (m26) 4584.0
4596.3	0.16	0.22	Fe II (m37) 4595.7
4608.1	0.23	0.37	N II (m5) 4607.2
4630.8	0.17	0.27	Fe II (m37) 4629.4
			N II (m5) 4630.5
4641.7	0.11	0.20	N III (m2) 4640.6
			O II (m1) 4641.8
			N III (m2) 4641.9

Table 4. continued.

Wavelength (Å)	$I_{obs}(\lambda)$	$I_{corr}(\lambda)$	Identification
4659.3	3.62	4.31	Fe III [m3F] 4658.1
4702.4	1.51	1.92	Fe III [m3F] 4701.5
4713.5	0.81	1.05	He I (m12) 4713.4
4734.4	0.71	0.86	Fe II (m43) 4731.4
4755.4	0.59	0.70	Fe III [m3F] 4754.7
4770.6	0.62	0.80	Fe III [m3F] 4769.4
4778.3	0.41	0.51	S II (m8) 4779.1
			N II (m20) 4779.7
4815.3	0.09	0.09	Fe II [m20F] 4814.6
4861.7	100.00	100.00	Hβ 4861.3
4881.3	0.16	0.19	Fe III [m2F] 4881.0
4904.8	0.20	0.23	Fe II [m20F] 4905.4
4922.5	1.72	1.97	He I (m48) 4921.9
			Fe II (m42) 4923.9
4930.5	0.42	0.43	Fe III [m1F] 4930.5
4959.0	63.49	55.37	O III [m1F] 4958.9
5001.1	0.32	0.26	N II (m19) 5001.1
5006.8	182.80	149.08	O III [m1F] 5006.9
5011.3	2.18	1.78	Fe III [m1F] 5011.3
5015.7	4.22	3.45	He I (m4) 5015.7
5018.4	0.28	0.23	Fe II (m42) 5018.4
5041.4	0.60	0.43	Si II (m5) 5041.1
5047.6	0.30	0.17	S II (m15) 5047.3
5055.8	0.56	0.30	Si II (m5) 5056.4
5084.4	0.21	0.19	Fe III [m1F] 5084.8
5158.9	0.31	0.21	Fe II [m18F] 5158.0
5168.1	0.26	0.18	Fe II (m42) 5169.0
5191.6	0.35	0.18	Ar III [m1F] 5193.3
5197.9	0.57	0.28	Fe II (m49) 5197.6
5233.9	0.36	0.26	Fe II (m49) 5234.6
5270.2	3.94	2.93	Fe III [m1F] 5270.4
5316.3	0.73	0.40	Fe II (m49) 5316.6
5332.7	0.27	0.10	Fe II [m19] 5333.7
5363.0	0.29	0.15	Fe II (m48) 5362.9
			Fe II [m17F] 5362.1
5375.1	0.13	0.06	Fe II [m19F] 5376.5
5411.5	0.41	0.21	Fe III [m1F] 5412.0
5425.4	0.12	0.05	Fe II (m49) 5425.3
5432.2	0.12	0.04	Fe II (m55) 5432.9
			Fe II [m18F] 5433.2
5475.6	0.26	0.05	Fe II (m49) 5477.7
5505.4	0.26	0.06	Cr III [m2F] 5505.1
5517.6	0.56	0.17	Cl III [m1F] 5517.2
5535.5	0.71	0.27	Cl III [m1F] 5537.7

Table 4. continued.

Wavelength (Å)	$I_{obs}(\lambda)$	$I_{corr}(\lambda)$	Identification
5551.3	0.43	0.10	N II (m63) 5552.5
5577.7	0.08	0.02	O I [m3F] 5577.4
5665.9	0.20	0.08	N II (m3) 5666.4
5677.8	0.39	0.16	N II (m3) 5676.0
5713.5	0.36	0.11	Fe II [m2F] 5713.4
5754.5	12.16	7.06	N II [m3F] 5754.8
5875.2	30.46	13.93	He I (m11) 5875.6
5956.8	0.47	0.21	Si II (m4) 5957.6
5978.8	0.79	0.33	Si II (m4) 5979.0
5999.8	0.35	0.12	Ni III 6000.2
6095.8	0.12	0.03	S II (m13) 6097.1
6124.5	0.23	0.06	S II (m13) 6123.4
6152.5	0.26	0.06	Cl II [m3F] 6152.9
6248.4	0.29	0.07	Fe II (m74) 6247.6
6300.4	1.93	0.77	O I [m1F] 6300.2
6312.0	12.84	4.57	S III [m3F] 6311.9
6347.1	1.06	0.35	Si II (m2) 6347.1
6364.0	0.67	0.23	O I [m1F] 6363.9
6371.4	0.72	0.25	Fe II (m40) 6369.5
			Si II (m2) 6371.4
6384.6	0.55	0.16	Fe II 6383.8
6401.4	0.26	0.07	Ni III 6401.5
6456.6	0.30	0.08	Fe II (m74) 6456.4
6483.2	0.17	0.05	Uid
6492.3	0.31	0.09	Fe II 6493.1
6516.9	0.12	0.03	Fe II (m40) 6516.1
6533.3	0.25	0.08	Ni III 6533.9
6548.1	26.90	7.49	N II [m1F] 6548.1
6563.0	1200.00	317.53	Hα 6562.8
6583.6	120.00	32.15	N II [m1F] 6583.6
6678.0	10.29	3.08	He I (m46) 6678.2
6716.2	0.51	0.14	S II [m2F] 6716.4
6730.5	1.25	0.33	S II [m2F] 6730.8
6746.9	0.15	0.04	Cr IV [m2F] 6746.2
6793.3	0.13	0.04	Fe I 6793.3
6826.9	0.15	0.03	Fe III 6826.2
6895.2	0.14	0.04	Fe II [m14F] 6896.2
6914.8	0.57	0.14	Cr IV [m2F] 6915.6
6944.9	0.15	0.03	Fe II [m43F] 6944.9
6996.2	0.31	0.07	[Fe IV] 6997.1
7001.9	0.14	0.03	O I (m21) 7001.9
7064.0	16.03	3.74	He I (m10) 7065.2
7087.3	0.11	0.03	Cr IV [m2F] 7087.1
7109.7	0.19	0.05	Uid

Table 4. continued.

Wavelength (Å)	$I_{obs}(\lambda)$	$I_{corr}(\lambda)$	Identification
7134.3	50.46	11.41	Ar III [m1F] 7135.8
7154.2	0.32	0.07	Fe II [m14F] 7155.1
7169.2	0.21	0.05	Fe II [m14F] 7171.9
7181.8	0.10	0.02	Fe II (m72) 7181.2
7232.9	0.74	0.14	Cr IV [m1F] 7233.4
7253.1	0.39	0.07	O I (m20) 7254.2
7279.7	2.03	0.41	He I (m45) 7281.4
7296.2	0.16	0.03	Uid
7317.9	57.34	11.19	O II [m2F] 7318.6
7328.2	48.95	9.56	O II [m2F] 7329.9
7375.8	0.31	0.06	Fe II 7376.5
7388.5	0.42	0.08	Fe II [m14F] 7388.2
7409.6	0.15	0.03	Si I (m23) 7409.1
7422.6	0.13	0.02	[Fe III] 7422.6
7431.2	0.27	0.04	Fe II 7431.35
7449.2	0.22	0.02	Fe II (m73) 7449.3
			Fe II [m30F] 7449.6
7465.8	0.23	0.03	Ni I [m2F] 7464.4
7478.1	0.13	0.02	Fe I 7478.9
7498.0	0.54	0.08	Fe II [m3F] 7497.7
7514.1	0.45	0.07	Fe II (m73) 7515.9
7712.2	0.59	0.10	Fe II [m30F] 7710.8
7751.0	14.91	2.30	Ar III [m1F] 7753.2
7775.1	0.46	0.08	O I (m1) 7775.4
7817.2	0.56	0.09	He I (m69) 7816.2
7868.9	0.42	0.05	Uid
7892.5	2.16	0.32	Uid
7917.8	0.82	0.10	Fe II [m29F] 7916.9
8131.6	0.34	0.04	Uid
8184.4	0.38	0.05	N I (m2) 8184.8
8309.7	0.19	0.02	Cr II [m1F] 8308.7
8317.6	0.24	0.03	Uid
8335.0	0.33	0.04	P24 8334.0
8345.7	0.50	0.05	P23 8346.0
8357.5	0.67	0.08	P22 8359.0
8372.9	1.22	0.14	Uid
8388.1	0.77	0.09	Uid
8406.4	0.83	0.09	Uid
8428.5	1.24	0.12	Uid
8453.6	1.01	0.11	Uid
8462.7	10.25	1.11	Uid
8484.2	1.67	0.15	Uid
8520.2	2.08	0.22	Uid
8566.3	1.84	0.19	Uid
8622.1	1.71	0.17	Uid